



OPEN Investigating the role of thrombosis and false lumen orbital orientation in the hemodynamics of Type B aortic dissection

Joseph C. E. Messou¹, Kelly Yeung², Eric Sudbrook³, Jackie Zhang^{4,5}, Shahab Toursavadkoshi⁴, Areck A. Ucuzian^{4,5,6} & Eleonora Tubaldi^{3,7,8}✉

While much about the fundamental mechanisms behind the initiation and progression of Type B aortic dissection (TBAD) is still unknown, predictive models based on patient-specific fluid-structure interaction (FSI) simulations can help in risk stratification and optimal clinical decision-making. Aiming at the development of personalized treatment, FSI models can be leveraged to investigate the interplay between complex aortic flow patterns and anatomical features, while considering the deformation of the arterial wall and the dissection flap. In this study, the hemodynamics of false lumen thrombosis, a large fenestration, and the orbital orientation of the false lumen is studied through image-based FSI simulations on three TBAD patient-specific geometries. A new pipeline is developed leveraging the open-source software SimVascular and ParaView to analyze multiple patients simultaneously and to achieve large-scale parallelization in FSI results based on patients' computed tomography (CT) images. The results of this study suggest that the internal orbital orientation of the false lumen contributes to maintaining a positive luminal pressure difference $\Delta P_{TL-FL} = P_{TL} - P_{FL}$ between the true lumen (TL) and the false lumen (FL), despite an impingement area in the false lumen near the entry tear. A positive and high luminal pressure difference is thought to promote TL expansion and FL compression. Moreover, it was also found that FL thrombosis at the entry tear region reduce the magnitude of the negative luminal pressure difference, which in turn may reduce FL expansion and the risk of unstable aortic growth. Finally, this FSI study suggests that the aortic wall and dissection flap stiffness determines the effects of a large fenestration in the descending thoracic aorta on the luminal pressure difference.

Acute Type B aortic dissection (TBAD) is a life-threatening condition caused by a primary tear in the aortic intima, which allows blood to flow through the aortic media. This results in aortic wall delamination and in the creation of a false lumen (FL) of blood flow. This secondary flow channel propagates longitudinally beside the original channel (i.e., true lumen, TL)^{1,2}, with the two lumens separated by a dissection flap. If left untreated, TBAD can lead to fatal complications such as chronic aneurysmal degeneration or acute organ malperfusion due to branch vessel ischemia³. With modern medical and surgical therapy, an increasing number of patients survive the TBAD acute state and enter the chronic phase of the disease where continued lifelong monitoring is needed to minimize the risk of morbidity and mortality. Surveillance imaging plays a pivotal role in assessing chronic TBAD disease progression and detecting late complications, such as aneurysm formation^{4,5}. Currently, the maximal aortic diameter is the principal determinant of long-term risk of rupture, though it is likely to be insufficient in precisely predicting future adverse events^{6,7}. Hemodynamic features, such as wall shear stress (WSS), oscillatory shear index (OSI), peak velocity, flow rate, and FL retrograde flow, could help identify early indicators of FL expansion and potential rupture.

¹Department of Electrical and Computer Engineering, University of Maryland, College Park, MD 20742, USA. ²Fischell Department of Bioengineering, University of Maryland, College Park, MD 20742, USA. ³Department of Mechanical Engineering, University of Maryland, College Park, MD 20742, USA. ⁴Division of Vascular Surgery, Department of Surgery, University of Maryland, Baltimore, MD 21201, USA. ⁵Center for Vascular and Inflammatory Diseases, University of Maryland, Baltimore, MD 21201, USA. ⁶Baltimore VA Medical Center, Vascular Service, Baltimore, MD 21201, USA. ⁷Division of Cardiology, College of Medicine, University of Maryland, Baltimore, MD 21201, USA. ⁸Robert E. Fischell Institute of Biomedical Devices, University of Maryland, College Park, MD 20742, USA. ✉email: etubaldi@umd.edu

Computational fluid dynamics (CFD) is a powerful tool to determine complex intra-aortic hemodynamics typical of TBAD patients^{8,9}. Image-based CFD simulations can predict the distribution of near-wall hemodynamic parameters with high resolution in arteries¹⁰. CFD patient-specific modeling and parametric studies have been successfully performed to explore the effects of specific parameters, such as boundary conditions¹¹, which affect the complex blood flow regime and flow-induced wall stresses^{12–14}. Recent CFD studies reported that FL growth correlates with low time-averaged WSS values in the distal false lumen^{15,16}, while in the region of the tear, high blood velocity and WSS values correlate with disease progression via FL dilation^{16–18}. Moreover, it was observed that a decreased velocity gradient at the entry tear, which results in a decreased time-averaged WSS, prevents the vessel from rupture¹⁹. Fewer fenestrations have been shown to potentially represent a predictor for unstable aortic growth²⁰. Similarly, a negative luminal pressure difference ($\Delta P_{TL-FL} = P_{TL} - P_{FL}$) is often associated with the expansion of the false lumen and the compression of the true lumen, while a positive and high pressure difference is thought to protect the true lumen from compressing^{21,22}. Recently, four-dimensional flow magnetic resonance imaging (4D Flow-MRI) has been increasingly used to provide non-invasive direct measurements of TBAD blood flow regimes^{23,24}. Despite the limited spatial and temporal resolutions, 4D Flow-MRI has a growing role in informing CFD boundary conditions^{25,26} and in validating CFD results²⁷. CFD simulations can also be leveraged to assess the effectiveness of treatment approaches and plan surgical interventions for TBAD²⁸. For instance, evaluating the impact of stent grafts after thoracic endovascular aortic repair (TEVAR) has the potential to become a practical pre-surgical tool^{22,29–31}. In particular, it has been shown that a large distance between the distal end of the stent-graft and the first post-stent re-entry tear (SG-FRT) could favor FL thrombosis³². In addition, aortic fenestration is an uncommon but possibly effective procedure for treating TBAD, by redirecting blood flow into the true lumen³³. However, there is currently not enough data to justify the routine use of the fenestration technique. Thus, CFD simulations can emerge as an important tool to properly select patients that would benefit from this treatment, as an alternative to aortic replacement^{34,35}. Finally, CFD simulations may provide insights into the hemodynamic consequences of fenestration coverage by endografts during TEVAR to the FL, TL, and distal organ vessels such as the mesenteric arteries³⁶.

While CFD simulations can provide important insights on hemodynamic factors related to aortic dissection, they rely on the assumption that the arterial wall and the dissection flap are rigid. This hypothesis can introduce inaccuracies in the results, especially in regions of expected high wall deformation, such as the false lumen, dissection flap, and entry tear^{37,38}. In order to incorporate the effects of small wall motion on the fluid dynamics without modeling the arterial wall, some studies have introduced the moving boundary method (MBM), which linearly relates the wall displacement and the pressure of the fluid^{39,40}. However, when more complex interactions between the fluid, the wall, and the flap are expected, fluid-structure interaction (FSI) models with both the fluid and the structural domain are needed. Recent works employed FSI simulations, both on idealized⁴¹ and patient-specific models⁴², showing that the motion of both the flap and the wall can highly impact the results. In particular, a more mobile flap can increase predicted thrombus volume by 25% due to the vortices near the tears⁴¹, and decrease the luminal pressure difference between the TL and the FL⁴². Overall, the state-of-the-art for FSI simulations of aortic dissection is rapidly evolving, with the potential of helping clinicians better understand complex hemodynamics while optimizing treatment outcomes.

Inspired by the growing role of FSI prediction models in advancing TBAD risk stratification and personalized care^{38,43}, this study analyzes the morphological and hemodynamic indices of three patients with different entry tear locations and false lumen orbital orientations. Patient-specific models are created to simulate physiological blood flow conditions with a moving arterial wall and dissection flap. In addition, in order to investigate how a large fenestration in the descending thoracic aorta and FL thrombosis affect TBAD hemodynamics, we compare three versions of the same patient's dissection considering (i) a large fenestration and a false lumen with thrombosis (original model), (ii) a primary entry tear and a false lumen without thrombosis nor fenestration, and (iii) a primary entry tear, a large fenestration, and a false lumen without thrombosis.

Methods

Patient-specific geometries

This study was reviewed and approved by the University of Maryland, Baltimore, Institutional Review Board (IRB). The need for informed consent was waived by the IRB of the University of Maryland, Baltimore. All data acquisition and methods were performed in accordance with relevant guidelines and regulations. Computer tomography (CT) angiography images of the chest, abdomen, and pelvis of three patients suffering from Type B aortic dissection were obtained per standard of care at the University of Maryland Medical Center using a Siemens SOMATOM Force CT scanner (see details in Supplementary Table s1) and retrospectively analyzed. The high-resolution CT images (ranging from 0.74 x 0.74 mm/pixel to 0.98 x 0.98 mm/pixel) were used to reconstruct the anatomic model of the dissected aorta for each patient (Fig. 1).

While all patients present a Type B_{3,x} aortic dissection⁴⁴, the geometry and size of the entry tear, as well as the distal extent of the dissection differ as reported in Supplementary Table s1. We refer to fenestrations at the distal extent of the dissection or in a branch as re-entry tears. Patient 1 presents a large entry tear (12.1 mm) while Patient 2's entry tear is relatively small (5.4 mm). As shown in Fig. 1, Patient 3's entry tear is obstructed by a thrombus in the false lumen that ends in the descending thoracic aorta. Patient 1's dissection extends to the paravisceral abdominal aorta, and the only re-entry tear is located distal to the celiac trunk. Patient 2's dissection extends into the abdomen, where the re-entry tears are located at the level of the left internal and external iliac arteries. While in Patient 1 the FL runs on the outer curvature of the aortic arch, in Patient 2 it runs on the inner curvature. Patient 3's dissection extends into the abdomen, where the re-entry tears are located in the aorta at the level of the left renal artery and the left external iliac artery. Several of the abdominal branch arteries are also dissected and the FL runs on the outer curvature of the aortic arch. The patient also has a large fenestration (3.7 mm) in the descending thoracic aorta, between the two cross-sectional areas DTA and DTA2 as shown in Fig. 1.

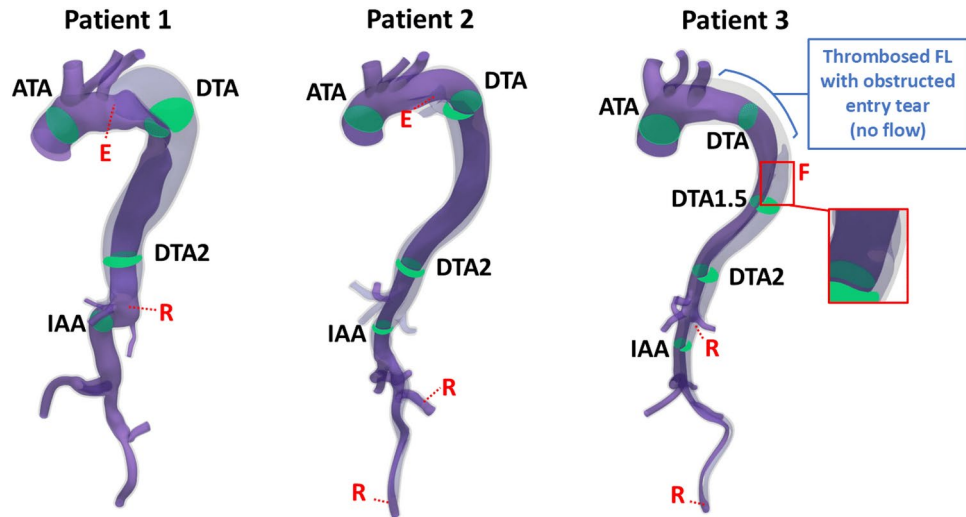


Fig. 1. Patient-specific Models. Patient-specific models with red labels denoting the entry tear (E), re-entry tear (R), and fenestration (F) locations. The following cross-sections at areas of interest are shown in green: ascending thoracic aorta (ATA), descending thoracic aorta (DTA/DTA1.5/DTA2), intra-abdominal aorta (IAA). Patient 3's large fenestration of 3.7 mm (red box) is located between the DTA and DTA2 cross-sections. The true lumen, the false lumen, and the solid are shown in purple, light purple, and grey, respectively. The location of the thrombus (i.e. no flow) in the false lumen (FL) of Patient 3 is highlighted in blue. Graphics generated using ParaView (v5.11, <https://www.paraview.org>).

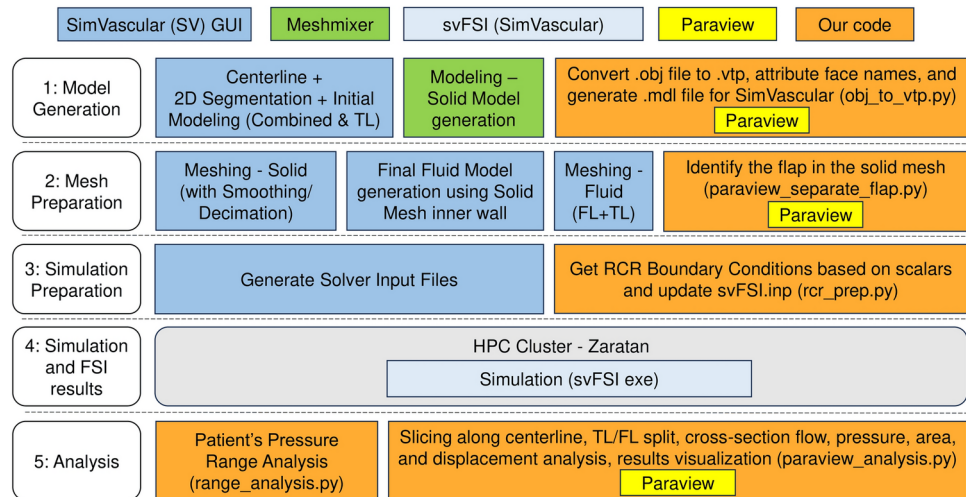


Fig. 2. CT-to-FSI Pipeline. Pipeline from patient's CT images to final FSI results. The code written to accelerate the pipeline and simplify the analysis of multiple patients is highlighted in orange.

Generation of fluid and solid meshes

As shown in Fig. 2, SimVascular⁴⁵, an open-source cardiovascular modeling and simulation software, was used to segment the CT images, model the fluid and solid domains, and simulate blood flow through the patient-specific geometries. The solid domain, also referred to as the structural domain, consists of the aortic wall and the dissection flap, while the fluid domain represents the region where blood flows. In FSI simulations, a separate mesh is needed for each domain, and a nodal interface between the two meshes is required. This constraint was enforced by adopting the methodology outlined by Bäumlner et al.⁴², where the procedure ensures that the wall of the fluid mesh and the inner wall of the solid mesh match. First, an initial fluid model was used to create the solid model following that procedure, then the solid model was meshed, and finally the inner wall of the solid mesh was used to create the final fluid model in SimVascular (Fig. 2).

Specifically, the solid domain was obtained by applying the following steps. The CT images were segmented to construct two separate surface models using SimVascular: one model with the TL alone and another including the TL, FL, and dissection flap, called the combined model. These models were exported to Meshmixer (Autodesk, Inc.), where the solid domain was generated. First, the TL and combined models were extruded assuming a

uniform wall thickness of 2 mm, except at the branches of the arch of Patient 2 and 3, where a wall thickness of 1 mm was used due to their proximity. Boolean operations were used to generate the FL model by subtracting the extruded TL model from the original combined model. The FL and original non-extruded TL were combined at the entry and re-entry tears to form the initial fluid domain, with a uniform dissection flap separating the TL and FL. The solid domain was obtained by subtracting the initial fluid domain from the extruded combined model. The solid model was then smoothed and re-meshed in Meshmixer before being exported to SimVascular for further smoothing operations with the goal of smoothing the bifurcations.

Due to the location of the entry tear in Patient 2 and the fenestration in Patient 3 (Fig. 1), this method was only applied from the bottom of the entry tear and fenestration to the iliac arteries. The upper part of the fluid domain was obtained separately in SimVascular by (1) segmenting the true lumen up to the tear, (2) segmenting the false lumen up to the tear, (3) segmenting the merged true and false lumens at the tear, and (4) combining 1, 2, and 3. The fluid model from the inlet to the tear and the fluid model from the bottom of the tear to the iliac arteries were then merged in Meshmixer before being used to generate the solid domain. For each patient, a tetrahedral mesh of the solid domain with a maximum edge size of 1.5 mm was created with the TetGen mesh generator⁴⁶ embedded in SimVascular. Similarly, tetrahedral meshes of the fluid domain with a maximum edge size of 2 mm, 1.5 mm, 1 mm, and 0.8 mm, and no inflation layers, were created.

Automatic flap identification within the solid domain

While the solid domain can be treated as a single domain, the aortic wall and the dissection flap tend to have different material properties⁴⁷. In order to assign a different elastic modulus to each region, the cells, or tetrahedral elements, of the dissection flap need to be identified before running FSI simulations. Towards this end, we have designed and implemented an automatic method as shown in Fig. 2. This new algorithm uses the inner-wall and outer-wall surface meshes of the solid to identify the dissection flap, and assigns a different *domain id* to the dissection flap and the aortic wall (Supplementary Algorithm s1). Given a volume mesh V of the solid domain, a surface mesh S_{in} of the inner wall, and a surface mesh S_{out} of the outer wall, the algorithm attributes the *domain id* 2 (aortic wall) or 3 (dissection flap) to every cell i of V using the points in S_{in} and S_{out} . It relies on the observation that cells in the aortic wall are surrounded by both the outer wall and the inner wall, while cells fully inside the dissection flap are surrounded only by the inner wall. As for cells at the boundaries of the dissection flap, they are mostly surrounded by the inner wall. Leveraging this observation, a cell i is first isolated so that it can only see the points in the inner wall and the outer wall, then the k -nearest points to the center of the cell are found. If at least one point of the outer wall is within the k -nearest points, the cell is considered part of the aortic wall, otherwise it is considered part of the flap. This approach is implemented by building a k -nearest neighbor⁴⁸ graph using the points in S_{in} and S_{out} and applying it to all the cell centers in V . After running the algorithm, the mesh is processed to guarantee that the flap is one contiguous domain. A feature was also added to let the user fix specific cells as the aortic wall for more complex flaps. For a small value of k , the algorithm will maximize the size of the flap, while for a larger value, it will be more conservative since there are more neighbors to look at to find the outer wall.

FSI simulations

Governing equations

Blood was modeled as an incompressible non-Newtonian fluid with a density $\rho_f = 0.00106$ g/mm³ and a shear-rate dependent viscosity⁴⁹. The viscosity was defined using the Carreau-Yasuda constitutive model⁵⁰ with parameters from Weddell et al.⁴⁹ (Supplementary Table s2). An arbitrary Lagrangian-Eulerian (ALE) formulation was used for the FSI equations^{42,51}, which accounts for the coupled deformation of the fluid and structural domains. The arterial wall and the dissection flap were given a density $\rho_s = 0.00102$ g/mm³ and were modeled as homogeneous, isotropic, nonlinear, hyperelastic materials using Neo-Hookean models^{42,52}. Each outlet of the structural domain was anchored using homogeneous Dirichlet boundary conditions, where the displacement field $\mathbf{u} = 0$. External tissue support was added to the outer arterial wall through a Robin-type boundary condition to factor in viscoelastic support^{42,53}:

$$\sigma_s \mathbf{n} = -k_s \mathbf{u} - c_s \partial_t \mathbf{u} - p_0 \mathbf{n} \quad (1)$$

where σ_s is the Cauchy stress tensor of the structural domain, \mathbf{n} the outward unit normal vector, and p_0 the external pressure in the thoracic and abdominal cavities. k_s and c_s model the elastic and viscoelastic response of the external tissue, respectively. Similar to Bäuml et al.⁴², we set $c_s = p_0 = 0$ and $k_s = 10^4$ g/(s·mm²). In order to maintain the scalability of the experiments, prestress was set to zero. As for the Young's modulus of the arterial wall E_{wall} and the Young's modulus of the dissection flap E_{flap} , they were both set to 800 kPa, which is within the acceptable range of the elastic modulus of the aorta^{47,54,55}. The effects of a more flexible flap were also explored with $E_{flap} = 100$ kPa.

Inlet flow rates and outlet RCR boundary conditions

A parabolic inlet flow waveform⁴² was tuned to match the patient-specific stroke volume (Fig. 3), which was derived using the CT images and echocardiogram reports. Using the left ventricular outflow tract (LVOT) Velocity Time Integral (VTI) from the echocardiogram reports and the LVOT area computed by direct planimetry from the CT images (Fig. 3), the stroke volume (SV) was computed as $SV(L) = LVOT_VTI (cm) * LVOT_Area (cm^2)$ ⁵⁶. Using this method yield stroke volumes of 161 mL (LVOT VTI = 37.6 cm, LVOT Area = 4.275 cm²), 134 mL (LVOT VTI = 36 cm, LVOT Area = 3.722 cm²), and 118 mL (LVOT VTI = 17 cm, LVOT Area = 6.962 cm²) for Patient 1, 2, and 3, respectively. As outlet conditions for each branch j , a three-element Windkessel model (or

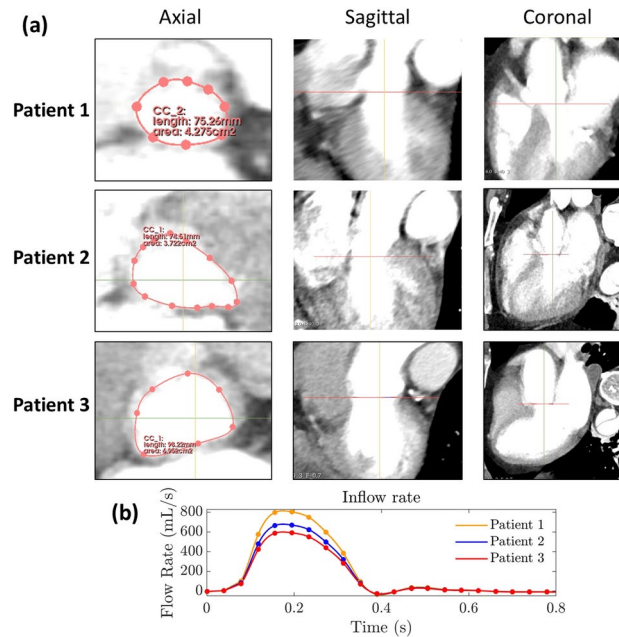


Fig. 3. LVOT Areas and Inlet Flow Rates. **(a)** Computed tomography (CT) images showing the left ventricular outflow tract (LVOT) Areas of Patient 1 (4.28 cm²), 2 (3.72 cm²), and 3 (6.96 cm²). The images are rotated so that the axial view is perpendicular to blood flow in the sagittal view. **(b)** Imposed inlet flow rate over one cardiac cycle ($t = 779$ ms). The stroke volume of each patient is used to scale the baseline inlet flow from Bäumlner et al.⁴², which corresponds to a stroke volume of 96.5 mL.

RCR) was applied using q_j , the fractional flow rate at the outlet obtained from Bäumlner et al.⁴² (Supplementary Table S3). The flow-proportional outlet resistance and capacitance are estimated by $R_{T,j} = R_T/q_j$ and $C_j = C_T \cdot q_j$, respectively, where R_T is the total resistance and C_T is the total capacitance. For each outlet, the distal and proximal resistance can be written as $R_{d,j} = k_d \cdot R_{T,j}$ and $R_{p,j} = (1 - k_d)R_{T,j}$, respectively, with $k_d = 0.9$ being the ratio of distal to total resistance^{42,57}. The Windkessel parameters were tuned for each patient on a medium-size mesh in order to obtain a systolic blood pressure (P_{sys}), a diastolic blood pressure (P_{dia}), a pulse pressure ($P_{sys} - P_{dia}$), and a mean arterial pressure ($(P_{sys} + 2 * P_{dia})/3$) within 7.7% of the patient-specific brachial cuff pressures (Supplementary Table S2).

Mesh convergence and FSI simulations

As shown in Fig. 2, FSI simulations were run using the open-source finite element-based solver svFSI⁵⁸, which is part of SimVascular. An optimal runtime was obtained using an iterative GMRES linear solver with a resistance-based pre-conditioner⁵⁹, both available in svFSI. Mesh convergence was accepted when the systolic blood pressure ($P_{inlet_{sys}}$) and the diastolic blood pressure ($P_{inlet_{dia}}$) at the inlet stayed within 2%. It was observed for a maximum edge size of 1 mm for all patients, and the final meshes of the full models had 6.5M, 4.9M, and 4.7M tetrahedral elements for Patient 1, 2, and 3, respectively. Final simulations were run for 1000 time steps per cardiac cycle with a step size of 0.779 ms to match a cardiac cycle period of 0.779 seconds. Cycle-to-cycle periodicity was reached within 4-7 cycles depending on the patient, and results are reported on the last cycle. As a reference, 1000 steps for a mesh of 4.9M tetrahedral elements ran approximately for 10h with a total of 256 cores split among multiple compute nodes (dual AMD 7763 64-core CPUs).

Efficient pipeline for tuning parameters

While SimVascular has an advanced graphical user interface (GUI) to compute the pressure and flow rate at the inlet and outlets, using the GUI can become a bottleneck when running large-scale experiments. In particular, depending on the target pressure tolerance, parameter tuning can take up to 10 runs of the numeral solver for a single patient. This involves (1) comparing the obtained pressure to the patient-specific blood pressure, (2) generating a new set of outlet boundary conditions, and (3) running the solver with the new set of parameters. As shown in Fig. 2, we developed scripts to efficiently tackle the aforementioned steps. The pressure range analysis script can automatically run after a simulation and compare the results to the patient-specific blood pressure. The user can then look at the relative differences and tune the parameters accordingly. Once the new scaling factors of the total resistance and capacitance are obtained, the user can then use one of the provided scripts to generate the new RCR boundary conditions and automatically update the solver's input file. As the number of patients studied grows, using the combination of these scripts will considerably improve the user workflow.

FSI solver results analysis

Once the final set of parameters has been chosen and the final FSI solver results are obtained, the next step is to visualize and analyze the data. To perform this efficiently while being consistent across multiple patients, we developed a script based on ParaView^{60,61}, as shown in Fig. 2. The script can be configured to automatically generate figures for the patient-specific models, such as WSS and OSI distributions, and velocity streamlines. In addition, given the centerline of the fluid model extracted from SimVascular, the script automatically makes slices perpendicular to the centerline and saves the coordinates of the slices. The user can then select the cross-sections of interest or process all slices. A feature specific to aortic dissection models was also added: the automatic detection of slices with two regions. When two regions are found in a slice, the script separates them as a large region and a small one and writes a file listing all small regions and their centroids. The user can then update that file and confirm if each small region at the given time step corresponds to the false lumen or not. During the final analysis, the FL and TL annotations are propagated to other time steps using the coordinates of the centroid of the small region. The regions can then be visualized as shown in the models of Fig. 4, or processed to compute the flow rate, the mean pressure, the FL and TL areas, and the maximum displacement of the FL, which are shown in the plots of Figs. 4 and s1. Overall, this script accelerates the visualization and processing of the FSI results, which is highly beneficial when multiple patients are involved in the study.

Results

Flow rate and pressure distributions

Figure 4a-c show results at different cross-sections over a cardiac cycle for Patient 1, 2, and 3, respectively. The graphs show the TL and FL blood flow rates Q_{TL} and Q_{FL} (mL/s), the luminal pressure difference ΔP_{TL-FL} (mmHg) = $P_{TL} - P_{FL}$, and the FL flow ratio FR_{FL} (%) = $100 \cdot (Q_{FL}/(Q_{TL} + Q_{FL}))$, with \bar{Q} denoting the average flow rate over time. The cross sections of interests are: the ascending thoracic aorta (ATA), descending thoracic aorta (DTA/DTA2), and intra-abdominal aorta (IAA).

In Patient 1 (Fig. 4a), the luminal pressure difference ΔP_{TL-FL} is minimal at DTA, but decreases before systole at DTA2, where the pressure in the FL is higher than the one in the TL by up to 8.8 mmHg. The FL flow rate is either higher than the TL flow rate or at least 80% of it at all times, with a FL flow ratio FR_{FL} of 59% at

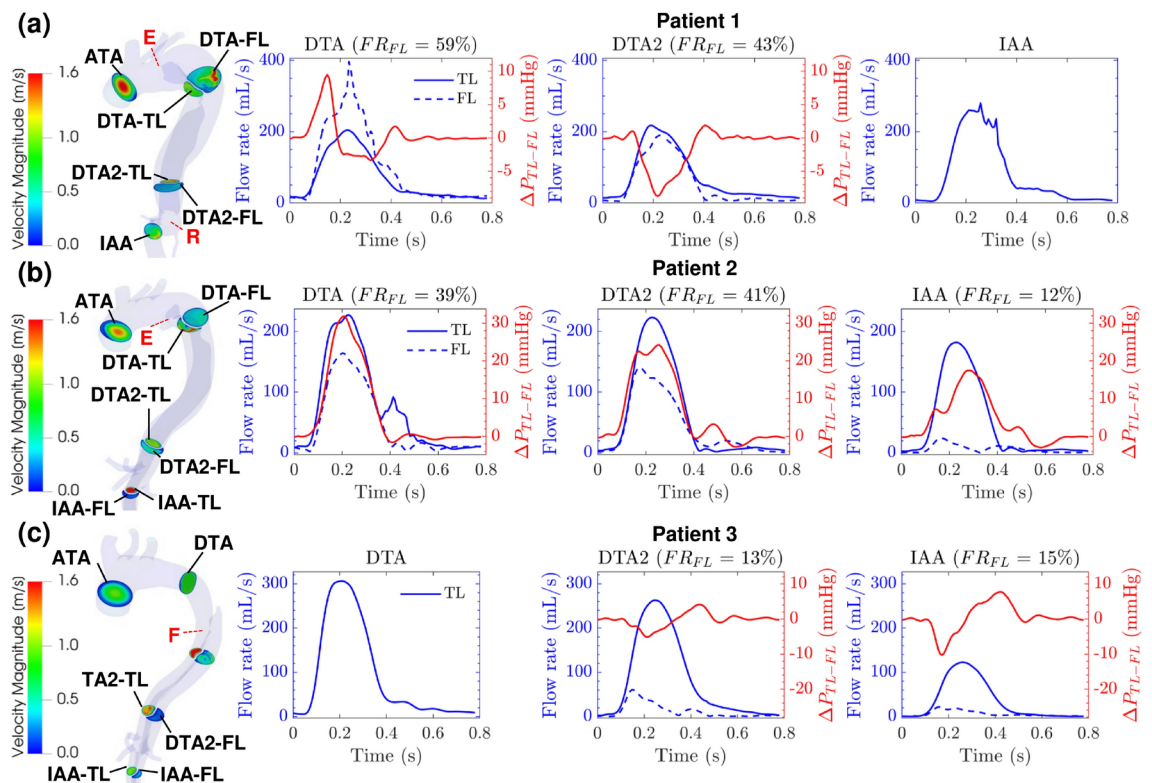


Fig. 4. Velocity magnitude, flow rate, and luminal pressure difference at key cross-sections Patient-specific models with cross-sections of interest colored by velocity magnitude at peak systole ($t = 234$ ms) for (a) Patient 1, (b) Patient 2, and (c) Patient 3. Red labels denote the location of the entry tear (E), re-entry tear (R), and large fenestration (F). The graphs show patients' true lumen (TL) flow rate (solid blue line), false lumen (FL) flow rate (dashed blue line), luminal pressure difference ΔP_{TL-FL} (red line), and FL flow ratio FR_{FL} at cross-sections of interest (DTA, DTA2, and IAA) over one cardiac cycle. Graphics generated using ParaView (v5.11, <https://www.paraview.org>).

DTA and 43% at DTA2. This is consistent with the large entry tear (12.1 mm) and the size of the dilated FL. On average, the FL area is 3.58x larger at DTA and 3.19x larger at DTA2 compared to the TL area.

In Patient 2 (Fig. 4b), all cross-sections present very high luminal pressure difference ΔP_{TL-FL} : 31.8 mmHg, 24.2 mmHg, 17.5 mmHg are found around peak systole at DTA, DTA2, and IAA, respectively. The TL flow rate is higher compared to the FL flow rate, and the cross-sectional areas are relatively similar except at DTA where the FL area is 2.4 smaller than the TL area, on average. Notably, the flow rate in the FL at IAA is much lower when compared to all other cross-sections. The FL flow ratio FR_{FL} is 39%, 41%, and 12% at DTA, DTA2 and IAA, respectively.

In Patient 3 (Fig. 4c), the luminal pressure difference ΔP_{TL-FL} is negative at DTA2 (-5.12 mmHg) and IAA (-10.3 mmHg) before peak systole, then increases during diastole up to 4.17 mmHg and 7.75 mmHg at DTA2 and IAA, respectively. While the FL and TL areas are comparable at DTA2, the FL flow rate is much lower than the TL flow rate, with a FL flow ratio of 13%. The FL flow ratio is similar at IAA despite the average FL area becoming 0.7x smaller than the average TL area.

For the three patients, the velocity magnitude at all cross-sections is higher in the TL than in the FL except at the DTA cross-section of Patient 2 where both lumens have comparable velocity magnitudes (Fig. 4).

Lumen areas and FL maximum displacement

Compared to CFD simulations where the wall is assumed to be rigid, FSI simulations take into account the displacement of the structural domain, which is composed of the arterial wall and the dissection flap. As shown in Fig. s1, the areas of the FL and TL vary before returning to their original values at the end of the cardiac cycle. Among the cross-sections, the magnitude of the displacement is the highest at DTA2 for all patients, specifically near the flap for Patient 1 and 3, and near the TL wall for Patient 2. Except at the DTA cross-section of Patient 2, the FL consistently shows a larger increase in area than the TL. Due to the high elastic modulus of the flap ($E_{flap} = 800$ kPa), the FL and TL maintain distinct sizes at all cross-sections, with one area remaining smaller than the other. The maximum magnitude of the FL's displacement at time $t_{max}(|d_{t,FL}|)$ peaks right after systole for Patient 1 and 3, while it is more even for Patient 2, meaning that there is less variation in the size of the FL for Patient 2. Patient 2 also exhibits a similar $max(|d_{FL}|)$ of 1.24 mm and 1.16 mm at DTA and DTA2, respectively.

Velocity streamlines

The velocity streamlines at peak systole ($t = 234$ ms) with a zoom on the flow behavior at the entry tear and large fenestration regions are shown in Fig. 5. A high-velocity flow jet that creates local recirculating flow in the FL is observed through the entry tear of Patient 1 and 2 and the large fenestration of Patient 3. Additionally, in both Patient 2 and 3, helical flow patterns are present in the FL distal to the entry tear and fenestration. In Patient 1, the FL flow velocity peak is found in the impingement area of the flow jet on the FL outer curvature wall. Similarly, the flow jet in Patient 2 creates an impingement area on the FL inner curvature wall. No impingement area is found in Patient 3. While the flow velocity in the FL increases in the vicinity of the tear and fenestration

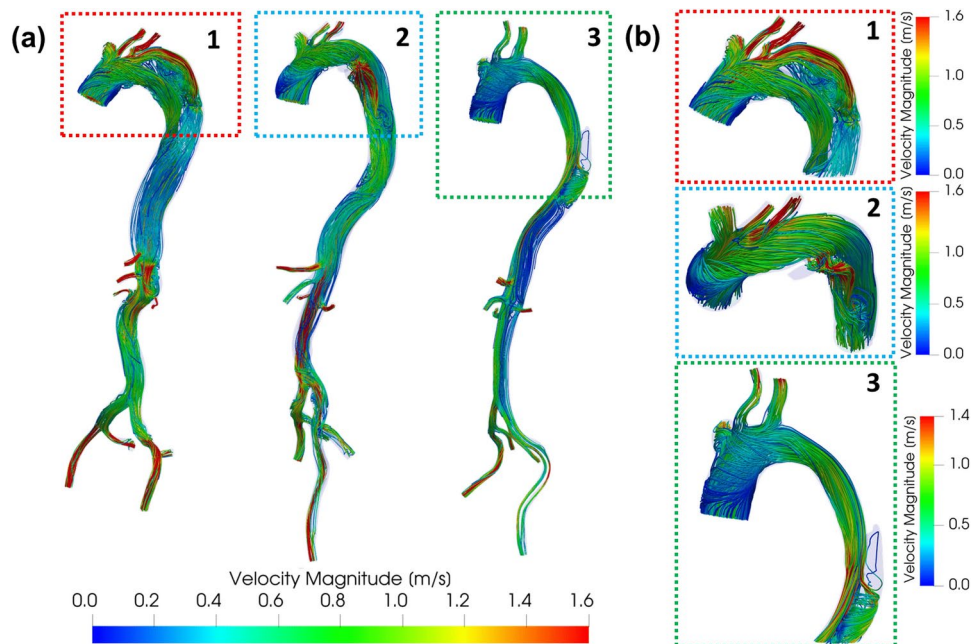


Fig. 5. Flow Velocity Streamlines. (a) Patients' velocity streamlines colored by velocity magnitude at peak systole ($t = 234$ ms). (b) Zoomed-in views of the aortic arch and entry tear/large fenestration showing: (i) a flow jet through the entry tear/large fenestration and (ii) a recirculating flow in the false lumen (FL). A helical flow can also be observed in the FL of Patient 2 and 3. Graphics generated using ParaView (v5.11, <https://www.paraview.org>).

for all patients, it reduces as the flow progresses down the thoracic aorta where it is much lower than the flow velocity in the TL.

TAWSS and OSI

Time-averaged wall shear stress (TAWSS), a measure of shear stress acting on the endothelial cells lining of the aortic wall averaged over the heartbeat cycle, and OSI, a dimensionless parameter quantifying the level of deviation of the WSS from its average direction, were computed for all patients as shown in Fig. 6a and b, respectively. In Patient 1, locally-high TAWSS values are observed in the proximity of the entry tear and re-entry tear regions. The FL impingement area of the flow jet through the entry tear corresponds to locally-high TAWSS. In the thoracic descending portion, the FL presents a general trend of low TAWSS and high OSI, and the opposite is found for the TL. In Patient 2, the FL presents a higher TAWSS in the thoracic aorta and it decreases in the abdominal aorta before increasing again in the iliac arteries. The FL impingement area of the flow jet through the entry tear corresponds to high TAWSS. In the TL, low TAWSS values are observed until the abdominal portion is reached. A peak in the OSI values is found in the TL in the vicinity of the entry tear and in the FL in the left external iliac artery. In Patient 3, the FL presents low TAWSS and high OSI distributions throughout the thoracic descending dissected portion. In the TL, TAWSS is high at the curvature of the descending aorta next to the large fenestration while OSI is high at the end of the curvature. The large fenestration presents a moderately high TAWSS and OSI.

Hemodynamic effects of different entry tear models for patient 3

In the two additional models of Patient 3, the thrombosed FL is considered as a part of the fluid domain with a primary entry tear of size 11 mm x 9 mm. As shown in Fig. 7, the original fenestration is removed in the first model (ET), and both the primary entry tear and the same large fenestration as the original model are considered in the second model (ET_FN). These new anatomic models both present an increase in the luminal pressure difference ΔP_{TL-FL} at DTA before peak systole, followed by a decrease to a negative value (Fig. 7). This behavior is accentuated in the ET model with a maximum ΔP_{TL-FL} of 13.1 mmHg and a minimum of -6.4 mmHg, while the maximum and minimum ΔP_{TL-FL} are 6.82 mmHg and -1.93 mmHg for the ET_FN model, respectively. The FL flow rate is also higher in the ET model. At DTA2 and IAA, ΔP_{TL-FL} and the flow rate of the new models (ET and ET_FN) follow similar trends as the original model of Patient 3 (Fig. 4). However, the range of ΔP_{TL-FL} decreases from the ET_FN model to the ET model, to the original model. Before peak systole, the FL pressure is higher than the TL pressure at DTA2 by 14.5 mmHg, 10.6 mmHg, and 5.12 mmHg in the

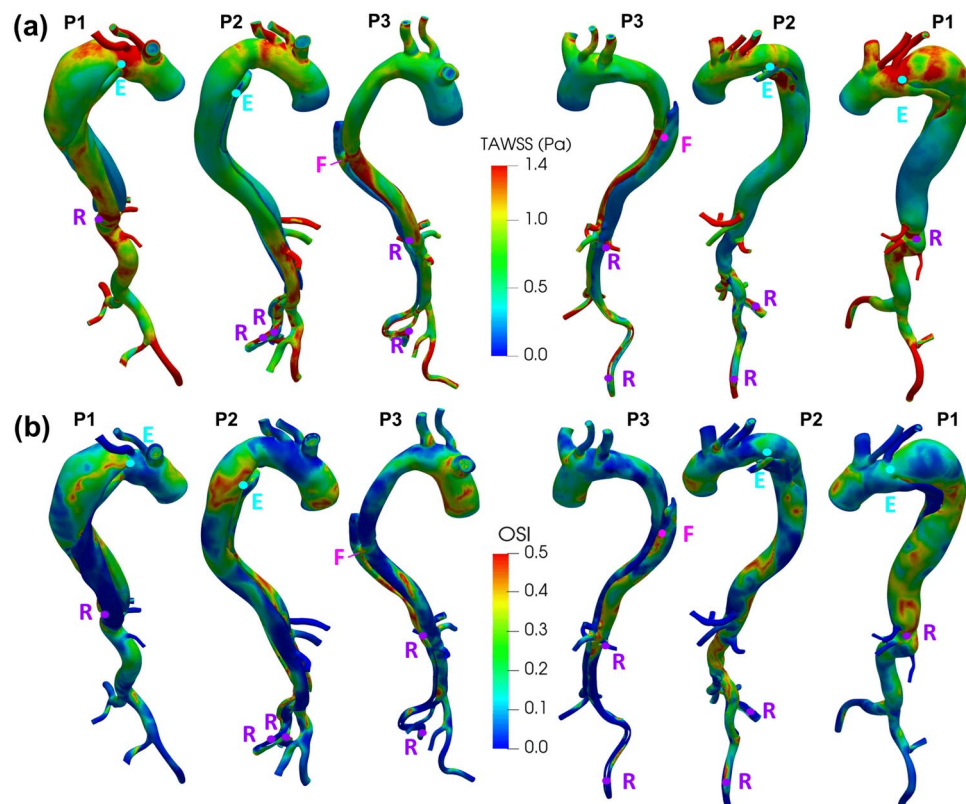


Fig. 6. TAWSS and OSI Distributions. (a) Time averaged wall shear stress (TAWSS) distribution and (b) oscillatory shear index (OSI) distribution for Patient 1 (P1), Patient 2 (P2), and Patient 3 (P3). (E) and (R) mark the entry and re-entry tear(s) locations, (F) marks the location of a large fenestration in the descending thoracic aorta of Patient 3. Graphics generated using ParaView (v5.11, <https://www.paraview.org>).

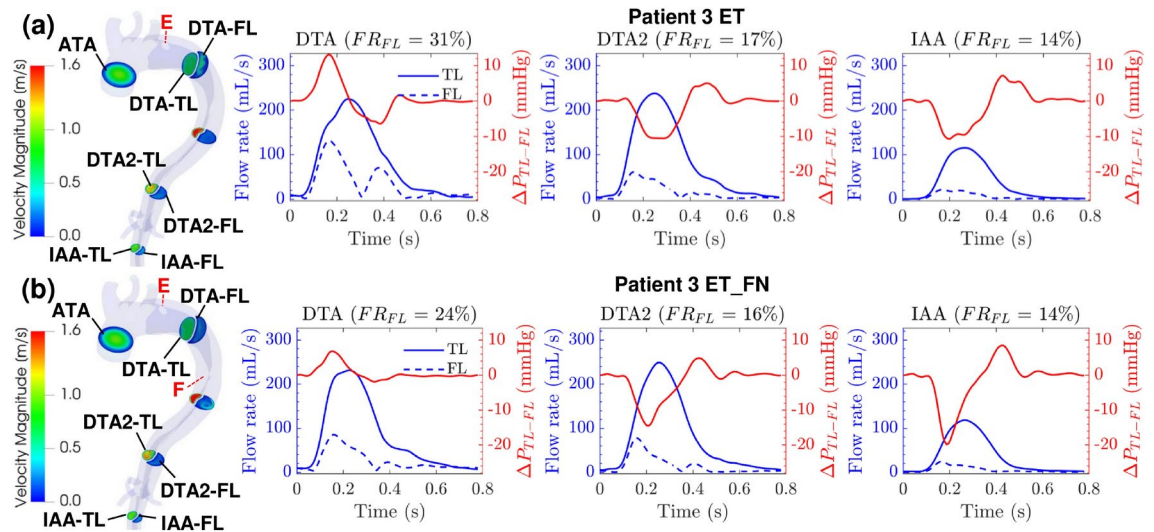


Fig. 7. Velocity Magnitude, Flow rate, and Luminal Pressure Difference at Key Cross-sections of Patient 3's Additional Models. **(a)** Patient 3's ET (entry tear only) and **(b)** ET_FN (entry tear and fenestration) models with cross-sections of interest by velocity magnitude at peak systole ($t = 234$ ms), and red labels denoting the location of the entry tear (E) and large fenestration (F). The graphs show the true lumen (TL) flow rate (solid blue line), false lumen (FL) flow rate (dashed blue line), luminal pressure difference ΔP_{TL-FL} (red line), and FL flow ratio FR_{FL} at cross-sections of interest (DTA, DTA2, and IAA) over one cardiac cycle. Graphics generated using ParaView (v5.11, <https://www.paraview.org>).

ET_FN, ET, and original models, respectively. The same trend is observed at IAA with a FL pressure higher than TL pressure by 19.9 mmHg, 10.8 mmHg, and 10.3 mmHg for the ET_FN, ET, and original models, respectively. While the FL flow ratio FR_{FL} at the DTA cross-section is 7% lower in the ET_FN model with respect to the ET model, it becomes comparable at the DTA2 and IAA cross-sections. The ET_FN and the ET models also have a higher displacement magnitude than the original model at the DTA2 cross-section (Supplementary Fig. s2). The maximum magnitude of the FL's displacement at IAA is 0.868 mm, 0.764 mm and 0.734 mm for the ET_FN, ET, and original models, respectively. The velocity streamlines for the ET and ET_FN models are shown in Fig. s3 of the Supplementary Material. A higher-velocity flow jet is present through the entry tear of the ET model which creates a stronger recirculating flow and an impingement area in the FL distal to the entry tear. At the fenestration in the ET_FN model, the flow goes from the FL to the TL differently with respect to the original model where we observe a flux from the TL to the FL (Fig. 5 and Supplementary Fig. s3). For the TAWSS and OSI distributions, all Patient 3 models follow a similar trend distal to the fenestration. Both ET and ET_FN models present an impingement area with high TAWSS in the proximity of the entry tear; higher TAWSS values are observed in the ET model (Supplementary Fig. s4).

Hemodynamic effects of the arterial wall and dissection flap stiffness on patient 3 Models

To assess the effects of the stiffness of the aortic wall and the dissection flap, the corresponding Young's moduli E_{wall} and E_{flap} were increased simultaneously from 0.8 MPa to 4 MPa for the three models of Patient 3 (i.e., original, ET_FN, and ET models). At the DTA cross-section near the entry tear, as E_{wall} increases, the range of the luminal pressure difference ΔP_{TL-FL} decreases from 8.75 to 4.89 mmHg for the ET_FN model and from 19.6 to 9.77 mmHg for the ET model (Fig. 8a). The opposite is observed at DTA2 and IAA where the range of ΔP_{TL-FL} increases for all models. In particular, the minimum ΔP_{TL-FL} of the ET model initially remains above that of the ET_FN model before dropping below it. This switch happens between 2 and 2.5 MPa at DTA, but it does not happen until 4 MPa at IAA. As for the original model, its minimum ΔP_{TL-FL} consistently exceeds that of the ET_FN and ET models. Figure 8b shows that as E_{wall} increases, the FL flow ratio FR_{FL} decreases at all cross-sections for all models, except at the IAA cross-section of the ET_FN model where it remains quite stable (within a 0.1% range). This indicates that a more mobile flap and wall send more blood into the FL. Especially at the DTA cross-section of the ET model, we can see that FR_{FL} decreases by more than 10% from the smallest elastic modulus to the largest. It initially remains above the FL flow ratio of the ET_FN model before falling below it starting at 2.5 MPa. The FL flow ratio at DTA shows a direct relationship with the range of ΔP_{TL-FL} at DTA and an inverse relationship with the range of ΔP_{TL-FL} at the DTA2 and IAA cross-sections.

Discussion

In the present study, hemodynamic parameters for three TBAD patients have been determined through patient-specific FSI simulations. All patients have an entry tear located distal to the left subclavian artery (Type B_{3,x}⁴⁴). Patient 1's re-entry tear is located distal to the celiac artery and proximal to the superior mesenteric artery. The false lumen runs on the outside of the aortic arch. Patient 2's re-entry tears are located at the level of the left internal and external iliac arteries. The false lumen runs on the inside of the aortic arch. Patient 3's re-entry tears

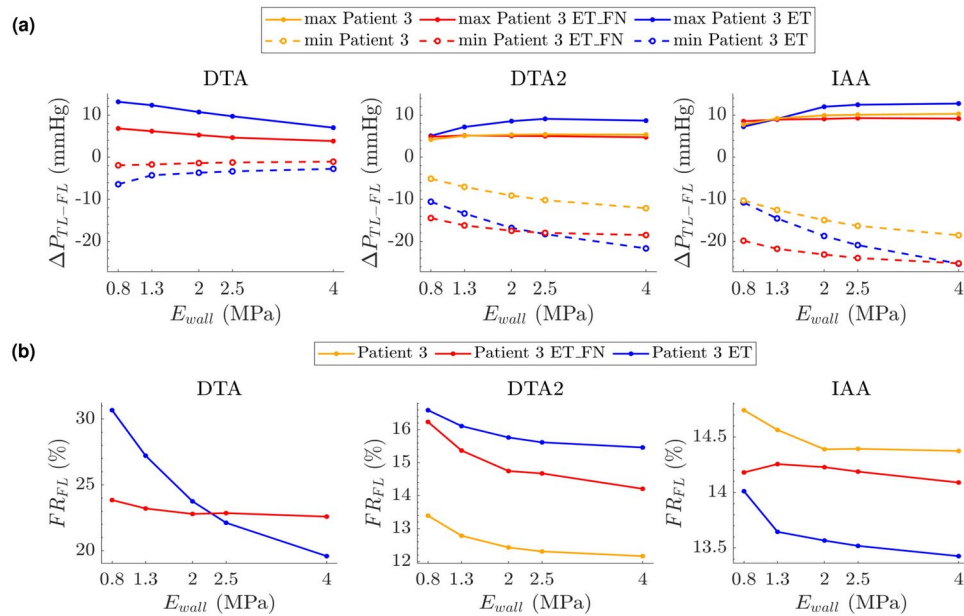


Fig. 8. Hemodynamic effects of the arterial wall and dissection flap stiffness on patient 3 Models. **(a)** Maximum (solid lines) and minimum (dash lines) of the luminal pressure difference ΔP_{TL-FL} and **(b)** false lumen (FL) flow ratio FR_{FL} of Patient 3's original model (yellow lines), ET_FN model (red lines), and ET model (blue lines) under an increasing elastic modulus E_{wall} , with $E_{flap} = E_{wall}$. Each column shows a different cross-section of interest (DTA, DTA2, and IAA).

are located at the left renal artery and the left external iliac artery. The false lumen runs on the outside of the aortic arch and is thrombosed up to the middle of the descending thoracic aorta. A large fenestration (3.7 mm) is located distal to the thrombus.

In the FL, Patient 1 presents high blood flow velocity, an impingement area, and high TAWSS distal to the entry tear, which correlate with a dilated false lumen. Indeed, the two cross-sections of the descending thoracic aorta have a FL area 3.58x (DTA) and 3.19x (DTA2) larger than the TL area on average. The FL flow ratios of 59% (DTA) and 43% (DTA2) also support the dilation of the FL. As for the luminal pressure difference, it is negative ($\Delta P_{TL-FL} = -8.8$ mmHg) at the DTA2 cross-section. A negative luminal pressure suggests the expansion of the FL and the compression of the TL since the FL has a higher pressure than the TL^{21,22}.

While the FL of Patient 2 also presents high blood flow velocity, an impingement area, and high TAWSS distal to the entry tear, it is mainly dilated at the tear and proximal to the tear. The FL area distal to the tear is 2.4x smaller than the TL area on average. This could be attributed to the location of the entry tear in the inner curve of the aorta, which creates a FL dilation towards the brachiocephalic trunk. Patient 2 also presents a high and positive luminal pressure difference at all cross-sections, with $\Delta P_{TL-FL} = 31.8$ mmHg at DTA before peak systole. This could help support the dissection flap and protect the TL from compression^{21,22}. The smaller size of the entry tear (Table s1) could also contribute to the high luminal pressure difference⁵¹, and in turn, to a more stable FL. This stability is also shown by a smaller variation in the size of the FL and a similar maximum FL displacement magnitude at DTA and DTA2. For Patient 3, lower FL flow velocity and TAWSS are observed in the fenestration region compared to the TL, which results in a more stable false lumen with a very low FL flow ratio of 13% and 15% at the DTA2 and IAA, respectively. Two anatomical features resulting in favorable hemodynamic indices seem to correlate with more stability and less growth of the FL: (i) the inner curve orientation of the false lumen (Patient 2) and (ii) the presence of a large fenestration²⁰ in the descending thoracic aorta when the arterial wall and the flap have a high stiffness (Patient 3). The first feature seems to maintain a positive luminal pressure difference, which protects the TL from compression. The second feature seems to reduce the magnitude of the negative luminal pressure difference, which minimizes the risk of FL expansion. The second feature is investigated using modified models of Patient 3 in the following section.

Thrombosis and fenestration

Anatomic features of the dissection, including the presence of fenestrations, may impact short-term and long-term TBAD outcomes. In addition, TEVAR by necessity and its nature has the effect of covering a number of fenestrations between the FL and TL. The impact of this coverage is often unpredictable in the clinical setting especially regarding its effects on perfusion for the distal organ vessels and the long-term remodeling of the TL and FL. To better investigate the effect of a large fenestration in the descending thoracic aorta and thrombosis in the FL, two additional models were created for Patient 3 neglecting the presence of the thrombus: (i) the ET model, a model without the fenestration and with an entry tear of size 11 mm x 9 mm distal to the subclavian artery, and (ii) the ET_FN model, a model with the same primary entry tear as the ET model and the same large fenestration as the original model. Hemodynamic parameters from each model were compared to investigate any significant

differences. As shown in Fig. 4 and 7, the general trend of the flow rate and luminal pressure difference ΔP_{TL-FL} is similar across all three models. The luminal pressure difference at DTA2 and IAA is first negative before the systolic peak, then positive at the beginning of diastole, and finally negligible. This means that the FL has a higher pressure than the TL before the systolic peak, which could lead to aneurysmal degeneration^{21,22}. Adding the fenestration in the ET model to obtain the ET_FN model increases FL pressurization as ΔP_{TL-FL} decreases by 3.87 mmHg and becomes more negative at DTA2. On the contrary, adding the thrombus in the ET_FN model to obstruct the entry tear, as shown in the original model, helps decrease FL pressurization as ΔP_{TL-FL} increases by 9.34 mmHg, becoming less negative. While the fenestration alone increases FL pressurization, the combination of the thrombus and the fenestration reduces it and brings ΔP_{TL-FL} closer to 0. This decrease in FL pressurization supports the natural formation of a thrombus and a large fenestration in Patient 3, which might protect Patient 3 from developing an aneurysm in the false lumen. As for the streamlines and the TAWSS of Patient 3's new models (Supplementary Figs. s3 and s4), they show the presence of an impingement area in the FL distal to the entry tear, which could lead to wall degeneration faster. This area has a lower flow velocity and a lower TAWSS in the ET_FN model compared to the ET model, most likely due to the flow being able to re-enter the true lumen through the fenestration. The potential threat that the impingement area causes is completely removed by the thrombus (i.e., no flow), while also reducing FL pressurization and FL displacement magnitude as previously discussed.

Reducing the elastic modulus of the dissection flap from 800 kPa to 100 kPa leads to the same conclusions for all patients (Supplementary Tables s4-s7). However, increasing the elastic modulus of the wall and the flap seems to determine the effect of the large fenestration on the luminal pressure difference. As shown in Fig. 8a, for $E_{wall} \geq 2.5$ MPa, the minimum luminal pressure difference becomes lower in the ET model compared to the ET_FN model. A similar shift can be observed at IAA for $E_{wall} = 4$ MPa. This suggests that as the aortic wall and the dissection flap become stiffer, the large fenestration in the descending thoracic aorta starts to help decrease FL pressurization by bringing the luminal pressure difference $\Delta P_{TL-FL} \sim 0$. This stiffness-dependent effect also highlights the importance of considering wall motion through FSI simulations to better represent physiological conditions.

Limitations

In this study, the baseline inlet flow rates and the outlet fractional flow rate values were obtained from Bäumler et al.⁴². Inaccuracies introduced in the patient-specific flow boundary conditions were mitigated by using a patient-specific stroke volume, which can be a good proxy to impose a patient-specific inlet flow profile¹¹. Ideally, a patient-specific 3D velocity profile at the inlet would be needed for more accurate results. Further inaccuracy was introduced with the assumption of a uniform dissection flap and a uniform aortic wall to simplify the generation of the solid and fluid models. Validation of the hemodynamic outcomes described in these results needs to be performed using corroborating studies including 4D-flow MRI scans to provide patient-specific flow, boundary conditions information, and TL/FL areas. However, the models in this study were developed using CT scans typically obtained in clinical settings at onset of the patients' acute presentation in the hospital emergency room. Therefore, validated predictions based on CT images obtained as standard of care, without the need for further studies using 4D-flow MRI information, could provide valuable and broadly accessible insights into patients' outcomes. In particular, outcomes resulting from anatomic features of the dissection, and the hemodynamic consequences of various interventions including TEVAR, which necessarily covers a number of fenestrations in addition to the entry tear, could be explored.

Conclusions

In this study, patient-specific FSI models have been obtained leveraging point of care CT images from three different patients suffering from acute Type B aortic dissection to investigate the role of FL thrombosis, fenestration, and false lumen orbital orientation. SimVascular⁴⁵ was used to create anatomic models and run simulations, and a custom code was developed to improve the scalability of aortic-dissection FSI analysis. In particular, this approach considerably accelerates (i) the tuning of the parameters to meet target pressures, (ii) FSI results visualization, and (iii) lumen cross-sectional analysis. The results show that thrombosis in the FL at the entry tear reduce the magnitude of the negative luminal pressure difference ΔP_{TL-FL} by 9.34 mmHg. Having similar luminal pressures in the TL and FL is thought to reduce the risk of FL expansion, hence promoting the formation of a stable false lumen^{18,62}. The presence of a large secondary fenestration in the thoracic aorta has a similar positive effect in the case of an arterial wall and dissection flap with high stiffness (i.e., $E_{wall} \geq 2.5$ MPa). However, the opposite behavior is observed when the aortic dissected walls are more compliant (i.e., $E_{wall} \leq 2$ MPa). Despite an impingement area in the false lumen near the entry tear, Patient 2 has a positive and high luminal pressure difference (up to $\Delta P_{TL-FL} = 31.8$ mmHg), which is thought to promote compression of the false lumen and expansion of the true lumen^{18,62}. The discrepancy between the impingement area and the high luminal pressure suggests that the orientation of the false lumen on the inner curve of the arch helps maintain a positive luminal pressure difference. This study demonstrates the potential of using FSI simulations in clinical settings to determine which anatomical features and hemodynamic characteristics are present in aortic dissections of varying severity. This approach can lead to a better understanding of the mechanisms behind TBAD progressive aortic growth dilatation and it can be leveraged to optimize treatment outcomes.

Data availability

The data that supports the results within this paper are available from the corresponding author upon reasonable request.

Code availability

The custom code of the proposed pipeline is available in the Github repository at (<https://github.com/jmessou/TBAD-CFD-Visualization>).

Received: 28 February 2024; Accepted: 30 October 2024

Published online: 09 November 2024

References

- Suzuki, T. et al. Clinical profiles and outcomes of acute type b aortic dissection in the current era: Lessons from the international registry of aortic dissection (irad). *Circulation* **108**, 312 (2003).
- Members, W. C. et al. 2022 acc/aha guideline for the diagnosis and management of aortic disease: A report of the american heart association/american college of cardiology joint committee on clinical practice guidelines. *J. Am. College Cardiol.* **80**, e223–e393 (2022).
- Luebke, T. & Brunkwall, J. Type b aortic dissection. *Aorta* **2**, 265–278 (2014).
- Nauta, F. J. et al. Update in the management of type b aortic dissection. *Vasc. Med.* **21**, 251–263 (2016).
- Zilber, Z. A. et al. Noninvasive morphologic and hemodynamic evaluation of type b aortic dissection: State of the art and future perspectives. *Radiol. Cardioth. Imaging* **3**, e200456 (2021).
- Sailer, A. M. et al. Computed tomography imaging features in acute uncomplicated stanford type-b aortic dissection predict late adverse events. *Circul. Cardiovasc. Imaging* **10**, e005709 (2017).
- Sailer, A. M. et al. Prognostic significance of early aortic remodeling in acute uncomplicated type b aortic dissection and intramural hematoma. *J. Thorac. Cardiovasc. Surg.* **154**, 1192–1200 (2017).
- Munshi, B., Parker, L. P., Norman, P. E. & Doyle, B. J. The application of computational modeling for risk prediction in type b aortic dissection. *J. Vasc. Surg.* **71**, 1789–1801 (2020).
- Madhavan, S. & Kemmerling, E. M. C. The effect of inlet and outlet boundary conditions in image-based cfd modeling of aortic flow. *Biomed. Eng. Online* **17**, 1–20 (2018).
- Johnston, L., Allen, R., Hall Barrientos, P., Mason, A. & Kazakidi, A. Hemodynamic abnormalities in the aorta of turner syndrome girls. *Front. Cardiovasc. Med.* **8**, 670841 (2021).
- Armour, C. H. et al. The influence of inlet velocity profile on predicted flow in type b aortic dissection. *Biomechan. Model. Mechanobiol.* **20**, 481–490 (2021).
- Romarowski, R. M., Lefieux, A., Morganti, S., Veneziani, A. & Auricchio, F. Patient-specific cfd modelling in the thoracic aorta with pc-mri-based boundary conditions: A least-square three-element windkessel approach. *Int. J. Numer. Methods Biomed. Eng.* **34**, e3134 (2018).
- Xu, H. et al. Computed tomography-based hemodynamic index for aortic dissection. *J. Thorac. Cardiovasc. Surg.* **162**, e165–e176 (2021).
- Osswald, A. et al. Elevated wall shear stress in aortic type b dissection may relate to retrograde aortic type a dissection: A computational fluid dynamics pilot study. *Europ. J. Vasc. Endovasc. Surg.* **54**, 324–330 (2017).
- Xu, H. et al. Coupled morphological-hemodynamic computational analysis of type b aortic dissection: A longitudinal study. *Ann. Biomed. Eng.* **46**, 927–939 (2018).
- Fatma, K., Carine, G.-C., Marine, G., Philippe, P. & Valérie, D. Numerical modeling of residual type b aortic dissection: Longitudinal analysis of favorable and unfavorable evolution. *Med. Biolog. Eng. Comput.* **60**, 769–783 (2022).
- Shang, E. K. et al. Use of computational fluid dynamics studies in predicting aneurysmal degeneration of acute type b aortic dissections. *J. Vasc. Surg.* **62**, 279–284 (2015).
- Zhu, Y. et al. Association of hemodynamic factors and progressive aortic dilatation following type a aortic dissection surgical repair. *Sci. Rep.* **11**, 11521 (2021).
- Abazari, M. A., Rafeianzab, D., Soltani, M. & Alimohammadi, M. The effect of beta-blockers on hemodynamic parameters in patient-specific blood flow simulations of type-b aortic dissection: A virtual study. *Sci. Rep.* **11**, 16058 (2021).
- Tolenaar, J. L. et al. Number of entry tears is associated with aortic growth in type b dissections. *Ann. Thorac. Surg.* **96**, 39–42 (2013).
- Cheng, Z., Wood, N. B., Gibbs, R. G. & Xu, X. Y. Geometric and flow features of type b aortic dissection: Initial findings and comparison of medically treated and stented cases. *Ann. Biomed. Eng.* **43**, 177–189 (2015).
- Xu, H. et al. Hemodynamic parameters that may predict false-lumen growth in type-b aortic dissection after endovascular repair: A preliminary study on long-term multiple follow-ups. *Med. Eng. Phys.* **50**, 12–21 (2017).
- Burris, N. S., Patel, H. J. & Hope, M. D. Retrograde flow in the false lumen: Marker of a false lumen under stress?. *J. Thorac. Cardiovasc. Surg.* **157**, 488–491 (2019).
- Wang, Q. et al.: Mri in cfd for chronic type b aortic dissection: Ready for prime time? *Comput. Biol. Med.* 106138 (2022).
- Black, S. M. et al. Calibration of patient-specific boundary conditions for coupled cfd models of the aorta derived from 4d flow-mri. *Frontiers in Bioengineering and Biotechnology* **11**, 1178483 (2023).
- Armour, C. H. et al. Evaluation and verification of patient-specific modelling of type b aortic dissection. *Comput. Biol. Med.* **140**, 105053 (2022).
- Wang, Q. et al. Computational fluid dynamic simulations informed by ct and 4d flow mri for post-surgery aortic dissection—a case study. *Int. J. Heat Fluid Flow* **96**, 108986 (2022).
- Marsden, A. L. Simulation based planning of surgical interventions in pediatric cardiology. *Phys. Fluids* **25**, 101303 (2013).
- Kan, X., Ma, T., Dong, Z. & Xu, X. Y. Patient-specific virtual stent-graft deployment for type b aortic dissection: A pilot study of the impact of stent-graft length. *Front. Physiol.* **12**, 718140 (2021).
- Li, Z. et al. The necessity to seal the re-entry tears of aortic dissection after tevar: a hemodynamic indicator. *Front. Bioeng. Biotechnol.* **10**, 831903 (2022).
- Polanczyk, A. et al. Computational fluid dynamic simulations in mimicking changes in blood hemodynamics in patients with acute type iiib aortic dissection treated with tevar. *Appl. Sci.* **8**, 1309 (2018).
- Armour, C. H., Menichini, C., Milinis, K., Gibbs, R. G. & Xu, X. Y. Location of reentry tears affects false lumen thrombosis in aortic dissection following tevar. *J. Endovasc. Thera.* **27**, 396–404 (2020).
- Panneton, J. M. et al. Aortic fenestration for acute or chronic aortic dissection: An uncommon but effective procedure. *J. Vasc. Surg.* **32**, 711–721 (2000).
- Pradhan, S., Elefteriades, J. A. & Sumpio, B. E. Utility of the aortic fenestration technique in the management of acute aortic dissections. *Ann. Thorac. Cardiovasc. Surg.* **13**, 296 (2007).
- Hartnell, G. G. & Gates, J. Aortic fenestration: A why, when, and how-to guide. *Radiographics* **25**, 175–189 (2005).
- Armour, C. et al. The role of multiple re-entry tears in type b aortic dissection progression: A longitudinal study using a controlled swine model. *J. Endovasc. Therapy* **31**, 104–114 (2024).

37. Alimohammadi, M. et al. Aortic dissection simulation models for clinical support: Fluid-structure interaction vs. rigid wall models. *Biomed. Eng. Online* **14**, 1–16 (2015).
38. Qiao, Y. et al. Numerical simulation of two-phase non-newtonian blood flow with fluid-structure interaction in aortic dissection. *Comput. Methods Biomech. Biomed. Eng.* **22**, 620–630 (2019).
39. Bonfanti, M. et al. Computational tools for clinical support: A multi-scale compliant model for haemodynamic simulations in an aortic dissection based on multi-modal imaging data. *J. Royal Soc. Interface* **14**, 20170632 (2017).
40. Bonfanti, M. et al. A simplified method to account for wall motion in patient-specific blood flow simulations of aortic dissection: Comparison with fluid-structure interaction. *Med. Engi. Phys.* **58**, 72–79 (2018).
41. Chong, M. Y. et al. An integrated fluid-structure interaction and thrombosis model for type b aortic dissection. *Biomechan. Model. Mechanobiol.* **21**, 261–275 (2022).
42. Bäuml, K. et al. Fluid-structure interaction simulations of patient-specific aortic dissection. *Biomechan. Model. Mechanobiol.* **19**, 1607–1628 (2020).
43. Luan, J. et al. The role of aorta distal to stent in the occurrence of distal stent graft-induced new entry tear: A computational fluid dynamics and morphological study. *Comput. Biol. Med.* **166**, 107554 (2023).
44. Lombardi, J. V. et al. Society for vascular surgery (svs) and society of thoracic surgeons (sts) reporting standards for type b aortic dissections. *Ann. Thoracic Surg.* **109**, 959–981 (2020).
45. Updegrave, A. et al. Simvascular: an open source pipeline for cardiovascular simulation. *Ann. Biomed. Eng.* **45**, 525–541 (2017).
46. Si, H. Adaptive tetrahedral mesh generation by constrained delaunay refinement. *Int. J. Numer. Methods Eng.* **75**, 856–880 (2008).
47. Amabili, M. et al. Biomechanical characterization of a chronic type a dissected human aorta. *J. Biomechan.* **110**, 109978 (2020).
48. Cover, T. M. & Hart, P. E. Nearest neighbor pattern classification. *IEEE Trans. Inform. Theory* **13**, 21–27. <https://doi.org/10.1109/TIT.1967.1053964> (1967).
49. Weddell, J. C., Kwack, J., Imoukhuede, P. & Masud, A. Hemodynamic analysis in an idealized artery tree: Differences in wall shear stress between newtonian and non-newtonian blood models. *PLoS one* **10**, e0124575 (2015).
50. Yasuda, K., Armstrong, R. & Cohen, R. Shear flow properties of concentrated solutions of linear and star branched polystyrenes. *Rheologica Acta* **20**, 163–178 (1981).
51. Zimmermann, J. et al. Hemodynamic effects of entry and exit tear size in aortic dissection evaluated with in vitro magnetic resonance imaging and fluid-structure interaction simulation. *Sci. Rep.* **13**, 22557 (2023).
52. Simo, J. *Computational Inelasticity* (Springer Science & Business Media, 2006).
53. Moireau, P. et al. External tissue support and fluid-structure simulation in blood flows. *Biomechan. Model. Mechanobiol.* **11**, 1–18 (2012).
54. Nichols, W. W., O'Rourke, M., Edelman, E. R. & Vlachopoulos, C. *McDonald's blood flow in arteries: theoretical, experimental and clinical principles* (CRC press, 2022).
55. Khanafar, K. et al. Determination of the elastic modulus of ascending thoracic aortic aneurysm at different ranges of pressure using uniaxial tensile testing. *J. Thoracic Cardiovas. Surg.* **142**, 682–686 (2011).
56. Liu, S. et al. Direct planimetry of left ventricular outflow tract area by simultaneous biplane imaging: Challenging the need for a circular assumption of the left ventricular outflow tract in the assessment of aortic stenosis. *J. Am. Soc. Echocardiogr.* **33**, 461–468 (2020).
57. Kim, H. J., Vignon-Clementel, I., Figueroa, C., Jansen, K. & Taylor, C. Developing computational methods for three-dimensional finite element simulations of coronary blood flow. *Finite Elements Anal. Des.* **46**, 514–525 (2010).
58. Zhu, C. et al. svfsi: A multiphysics package for integrated cardiac modeling. *J. Open Sour. Softw.* **7**, 4118 (2022).
59. Esnaily-Moghadam, M., Bazilevs, Y. & Marsden, A. L. A new preconditioning technique for implicitly coupled multidomain simulations with applications to hemodynamics. *Computat. Mech.* **52**, 1141–1152 (2013).
60. Ahrens, J., Geveci, B., Law, C., Hansen, C. & Johnson, C. 36-paraview: An end-user tool for large-data visualization. *Visualiz.* **717**, 50038 (2005).
61. Ayachit, U. *The paraview guide: a parallel visualization application* (Kitware, Inc., 2015).
62. Ab, W. A. N. et al. The impact of the number of tears in patient-specific stanford type b aortic dissecting aneurysm: Cfd simulation. *J. Mech. Med. Biol.* **14**, 1450017 (2014).

Acknowledgements

We acknowledge the support of the University of Maryland, Baltimore, Institute for Clinical & Translational Research (ICTR) and the National Center for Advancing Translational Sciences (NCATS) Clinical Translational Science Award (CTSA) grant number UL1TR003098 (A.A.U.). We also acknowledge the support of the NIH Grant K08 HL146893 (A.A.U.) and the SVS Foundation/American College of Surgeons Mentored Clinical Scientist Research Career Development Award (A.A.U.). We also acknowledge the University of Maryland supercomputing resources (<http://hpcc.umd.edu>) made available for conducting the research reported in this manuscript.

Author contributions

J.C.E.M. and E.S. segmented the CT images and modeled the fluid and solid domains. J.C.E.M. performed FSI simulations and wrote the code to accelerate the pipeline and analyze the FSI intermediate results. J.C.E.M., K.Y., and E.T. prepared the figures. J.Z. and A.A.U. obtained and reviewed the CT images. J.C.E.M., A.A.U., S.T., and E.T. conceptualized the study and analyzed the results. J.C.E.M. and E.T. wrote the manuscript with input from all authors. All authors reviewed the manuscript.

Declarations

Competing Interests

The authors declare no competing interests.

Additional information

Supplementary Information The online version contains supplementary material available at <https://doi.org/10.1038/s41598-024-78348-9>.

Correspondence and requests for materials should be addressed to E.T.

Reprints and permissions information is available at www.nature.com/reprints.

Publisher's note Springer Nature remains neutral with regard to jurisdictional claims in published maps and institutional affiliations.

Open Access This article is licensed under a Creative Commons Attribution-NonCommercial-NoDerivatives 4.0 International License, which permits any non-commercial use, sharing, distribution and reproduction in any medium or format, as long as you give appropriate credit to the original author(s) and the source, provide a link to the Creative Commons licence, and indicate if you modified the licensed material. You do not have permission under this licence to share adapted material derived from this article or parts of it. The images or other third party material in this article are included in the article's Creative Commons licence, unless indicated otherwise in a credit line to the material. If material is not included in the article's Creative Commons licence and your intended use is not permitted by statutory regulation or exceeds the permitted use, you will need to obtain permission directly from the copyright holder. To view a copy of this licence, visit <http://creativecommons.org/licenses/by-nc-nd/4.0/>.

© The Author(s) 2024